NANO LETTERS

2007
Vol. 7, No. 9
2596−2601

Strain and Shape of Epitaxial InAs/InP Nanowire Superlattice Measured by Grazing Incidence X-ray Techniques

Joël Eymery,* François Rieutord, Vincent Favre-Nicolin, Odile Robach, Yann-Michel Niquet, Linus Fröberg, Thomas Mårtensson, and Lars Samuelson

CEA Grenoble, Département de Recherche Fondamentale sur la Matière Condensée, Service des Matériaux et Microstructures, 17 rue des Martyrs, 38054 Grenoble Cedex 9, France, and Solid State Physics, Lund University, Box 118, S-221 00 Lund, Sweden

Received April 16, 2007; Revised Manuscript Received July 26, 2007

ABSTRACT

Quantitative structural information about epitaxial arrays of nanowires are reported for a InAs/InP longitudinal heterostructure grown by chemical beam epitaxy on an InAs $(111)_B$ substrate. Grazing incidence X-ray diffraction allows the separation of the nanowire contribution from the substrate overgrowth and gives averaged information about crystallographic phases, epitaxial relationships (with orientation distribution), and strain. In-plane strain inhomogeneities, intrinsic to the nanowires geometry, are measured and compared to atomistic simulations. Small-angle X-ray scattering evidences the hexagonal symmetry of the nanowire cross-section and provides a rough estimate of size fluctuations.

The development of vertical semiconductor nanowires (NW) as new building blocks for future nanoscale electronics and photonics devices is strongly dependent on the crystalline quality. For some applications (like field effect transistors), the properties of individual (and identical) NWs must be mastered, whereas in other applications, device operation depends on the characteristics of a number of NW in parallel and therefore on the distribution width of the assembly. For example, resonant sensors or optical microcavities containing many NWs must have well-matched diameters to obtain a high quality factor.

To characterize the structural properties of these new materials, transmission electron microscopy (TEM) is a standard tool that gives first-rate information about individual objects or small assemblies including the determination of the growth directions, heterostructure cross sections, surface facets, dislocations, or stacking faults.[1,2] In spite of their very strong complementarities with TEM, X-ray diffraction techniques are up to now very seldom used to get averaged quantitative information important for practical use. Experiments on epitaxial arrays to study defects, disorientations, and strains are very limited,[3−6] and only powder diffraction or texture methods are routinely performed on broadly oriented NW growths. In this paper, we will show that with the development of the growth control, epitaxial NW heterostructures can now be effectively studied by conventional synchrotron X-ray scattering techniques,[7] i.e., grazing incidence X-ray diffraction (GIXRD) and small-angle X-ray scattering (SAXS). It will be shown that statistical quantitative information can be obtained concerning epitaxial relationships, orientation distributions, strain relaxation, and stacking defects. These points will be illustrated by the detailed analysis of a 20 period InAs/InP nanowire superlattice, including comparison to simulation.

The nanowire growth is Au-assisted and takes place in a chemical beam epitaxy (CBE) system using trimethylindium, precracked *tert*-butylarsine, and precracked *tert*-butylphosphine as growth precursors.[8] Prior to growth, size-selected Au aerosol particles are deposited on a InAs(111)B substrate and the sample is deoxidized in the growth chamber at 520 °C under As pressure. Growth is started at 425 °C for about 530 nm of InAs and then further lowered to 390 °C for the superlattice growth with 20 segments of 20 nm (InAs) and 10 nm (InP). The structure is ended with an InAs segment of about 65 nm.

Figure 1 shows scanning electron microscopy (SEM) images of the sample, indicating that most of the NWs are perpendicular to the surface with a standard hexagonal cross section. TEM analysis shows $\langle 11\bar{2}\rangle$ side facets referred to the cubic substrate and a Wurtzite structure of the nanowire; we have never seen any cubic insertion at the bottom of the nanowire or anywhere else.[8] On top of the surface, small pyramidal hillock overgrowths can be observed (see Figure 1b,e). The narrow NW orientation distribution allows studying the NW reciprocal space according to the substrate lattice, and the (*hkl*) Miller indexes, corresponding to the InAs $(111)_B$

* Corresponding author. E-mail: joel.eymery@cea.fr. Équipe Mixte CEA-CNRS-UJF, Nanophysique et Semiconducteurs, CEA Grenoble.

10.1021/nl070888q CCC: $37.00
Published on Web 08/28/2007

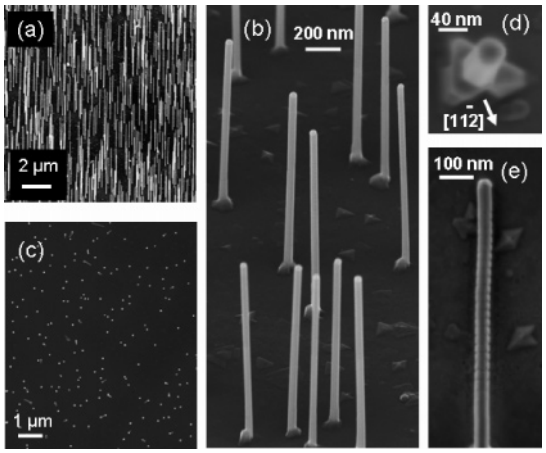

Figure 1. Scanning electron microscopy images of CBE grown epitaxial nanowires. (a,b) tilted views, (c,d) top views, showing the vertical alignment and the hexagonal cross section with facets corresponding to the [11$\bar{2}$] direction indexed in the cubic substrate lattice; (e) side view, where the superlattice periods are barely seen (see cover picture for a SEM picture in the transmission geometry).

surface unit cell, can be used as a reference. The surface unit cell lattice vectors have a hexagonal basis $\mathbf{a}_1$, $\mathbf{a}_2$, $\mathbf{a}_3$ with $\mathbf{a}_1 = {}^1/_2[\bar{1}10]$, $\mathbf{a}_2 = {}^1/_2[0\bar{1}1]$ in the surface plane, and $\mathbf{a}_3 =$ [111] perpendicular to the surface. The corresponding reciprocal lattice vectors are along three *h*,*k*,*l* axes with *h* and *k* in the surface plane, making an angle of 60° and *l* normal to the surface. In these coordinates, InAs $(111)_B$ bulk Bragg reflections are found at $l = 1, 4, 7, \ldots$ for $(h,k) = (1,0)$ and at $l = 2, 5, 8, \ldots$ for $(h,k) = (0,1)$. X-ray experiments were performed at the European Synchrotron Radiation Facility (ESRF, Grenoble France) under helium flow to prevent sample degradation and to avoid background diffuse scattering from the air. Diffraction (respectively, small angle) data were collected on the BM32 French CRG beamline using 10 (respectively, 18) keV photon energy. The beam footprint on the sample surface, which is about 5 × 0.5 (0.1) mm^2, integrates the intensities of a very large number of NWs.

Figure 2 shows the measurements of the (01*l*) crystal truncation rod (CTR) for several grazing incidence angles α. Close to the substrate critical angle for total external reflection ($\alpha_c = 0.29°$), we measure at $l = 2$ and 5 the sharp and intense diffraction peaks of the InAs substrate (labeled S). Their intensities decrease with decreasing α and vanish in the "transmission" geometry ($\alpha = 0°$). The extra peaks may come either from the NWs or from other surface overgrowths. Peak intensities at $l \approx 1.5$, 3, and 4.5 (labeled NW in Figure 2) do not depend on the incidence angles, whereas some "satellites" at $l \approx 1$, 2, 4, and 5 (labeled TW, for twinned overgrowth) do. This strongly suggests that noninteger peaks can be attributed to the NWs. It is confirmed by the peak-shape dependence on the incidence shown in the inset of Figure 2. In the transmission geometry and for α close to the critical angle, only a single peak is measured. In intermediate cases, a second peak is measured. Its larger-angle position depends on α, and at $\alpha = 0.1°$, the two peaks overlap. These observations can be explained by using the distorted-wave Born approximation (DWBA). In

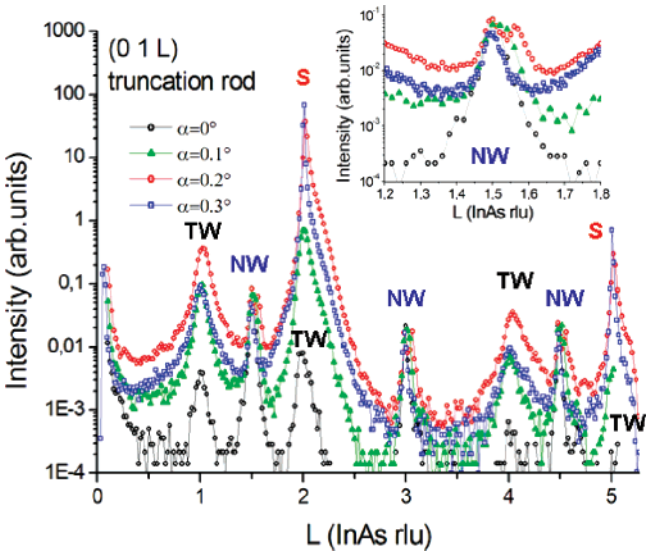

Figure 2. (01*l*) crystal truncation rod measurement for several grazing incidences ($\alpha = 0$, 0.1, 0.2, 0.3°). *l* is in reciprocal lattice units (rlu) of the cubic InAs(111) substrate (marked by S). NW (TW) correspond to the nanowires (substrate overgrowths) peaks. Inset: splitting of NW-peak at $l = 1.5$ in two contributions as the function of α. This effect is explained in the text by the coexistence of several scattering processes at very grazing angle.

this formalism, the scattered wave amplitude is composed of four terms, including all combinations of scattering from the NW and reflection from the substrate.[9] At very low grazing incidence (transmission geometry), the incident beam is scattered by the NW and collected by the detector, whereas at larger α (but lower than α_c), a second contribution comes from the reflection by the surface toward the NW. This reflection acts as a second "incident beam" with a wave vector pointing slightly upward. The surface reflection is sharply decreased for $\alpha > \alpha_c$, which explains why the two terms are observed only at very grazing angle. The third and fourth term considered in DWBA, coming respectively from the beam scattered by the NW and reflected by the surface and from both incident and scattered beam reflected by the surface, are negligible because downward scattered beams have an angle much larger than α_c with respect to the surface. This multiple scattering effect also applies to the TW peaks, and a small shift is observed with α, but peak broadness causes the two contributions to overlap. The TW peaks intensities decrease with the incidence suggesting a different origin.

To have more insights about the nature of these peaks, we measure for $\alpha = 0.3°$ several CTRs in the (*h*0*l*), (0*kl*), and (*hhl*) reciprocal planes (see some examples in Figure 3b,c). Figure 3a summarizes the (*h*0*l*) measurements referred to the InAs cubic substrate lattice. Zinc-blende InAs substrate and hexagonal NWs peaks are easily indexed by considering the stacking sequence of (111) planes.[6] Note that two variants having the same peak intensities are measured for the hexagonal NWs. They correspond to "equivalent" 60° rotations domains, which can be probably attributed to different NWs orientations on the (111) surface. TEM observations rule out defects in individual NWs, moreover, this kind of defect should not give identical domains

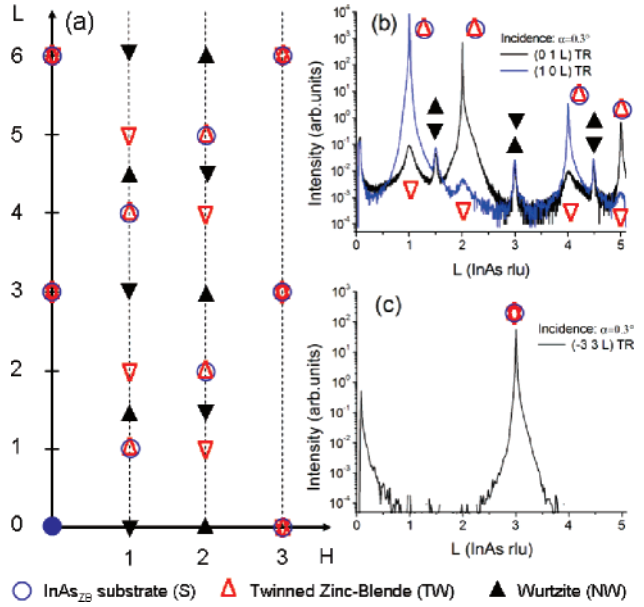

Figure 3. (a) Schematics of the (*h*0*l*) reciprocal plane of the sample shown in Figure 1 (*h*,*l* scales and peak positions are only indicative): (○) InAs cubic substrate, (▲▼) hexagonal NW variants obtained by 60° in-plane rotations, (△▽, in red) twinned cubic substrate overgrowth (ACB stacking of the (111) planes instead of ABC). (b,c) Truncation rod measurements examples (*l* scans) for α = 0.3°: (b) along (10*l*) and (01*l*) (equivalent to (20*l*) in (a)), and (c) along (−33*l*).

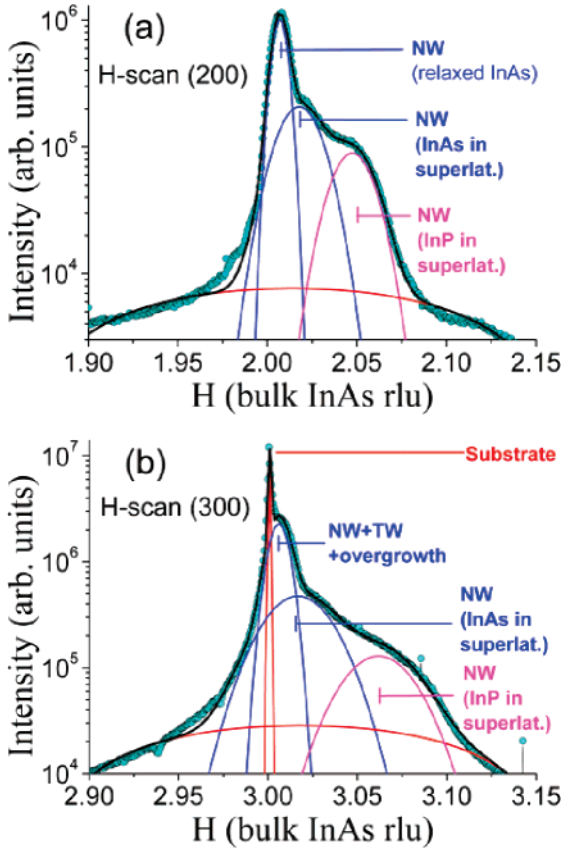

Figure 4. In-plane measurements along *h* (see the definition in Figure 3) for the (a) (200) and (b) (300) reflections. Points correspond to measurements and thick curves to the best fits of the nanowires (NW), twinned overgrowth (TW), and substrate (S) contributions. *h* is in reciprocal lattice units (rlu) of the cubic InAs-(111) substrate.

intensities. The TW peaks are consistent with twins of a cubic phase having a lattice parameter close to the substrate. They can be attributed to the pyramidal hillocks observed by SEM (see Figure 1b,e) in agreement with the α-dependence shown in Figure 2 and with the in-plane orientation distribution (mosaicity) discussed later. The hillock morphology is commonly observed in zinc-blende (111) epilayers for II−VI and III−V compounds. This structure may be nucleated on a surface defect (for example on a gold contamination coming with the aerosol catalysts). The stable cubic phase is obtained due to the strong coupling with the surface. Indeed, we do not have the influence of the NW geometry (dimension and surface effects) that could stabilize the metastable hexagonal structure. The NW and TW lattice parameters are deduced both from in-plane ⟨200⟩, ⟨300⟩, and out-of-plane ⟨01*l*⟩ measurements according to the cubic phase reference ($a_{\mathrm{Subst}}^{\mathrm{InAs}} = 0.60583$ nm and $a_{\mathrm{Subst}}^{\mathrm{InP}} = 0.58687$ nm).

As shown in Figure 4, the fit of in-plane measurements (reflections perpendicular to the surface) allows determination of the different contributions to the measured intensity: the substrate overgrowths, the relaxed InAs segments at the bottom and the top of the nanowire, and the average InAs and InP insertions in the superlattice. For the sake of simplicity, we chose a Gaussian function to model the Bragg peak shape. This choice is adequate to describe the center position and the width of the peak, but it is surely not enough to describe the peak tails. A more complicated description (with more parameters to fit) should take into account these features. It should probably decrease the background below the signal (see the red curve in Figure 4), but up to now no strong physical argument can be given to select the function type (Lorentz, Voigt, Pearson...). Wurtzite InAs NW position (shown in (200) *h* scan and in Figure 3) is slightly larger than the cubic InAs substrate. It corresponds to the bottom and to the top of the NW and should be relaxed due to the small NW diameter and to the small lattice mismatch: the in-plane lattice parameter is only decreased of about 0.32% ± 0.03 according to the substrate reference. For the (003) measurement (see Figure 4b), the relaxed InAs NW signal is superposed to the TW contribution and eventually to planar (and not twinned) substrate overgrowth. The fit of this composite peak gives 0.17% ± 0.03, suggesting that the two last phases are very close to bulk cubic InAs. For the NW superlattice, the InAs and InP average in-plane lattice parameters can be estimated by the positions of the peak maxima of (002) and (003) *h* scans: $a_{\mathrm{NW}}^{\mathrm{InAs}}/a_{\mathrm{Subst}}^{\mathrm{InAs}} = 0.9936 \pm 0.001$ and $a_{\mathrm{NW}}^{\mathrm{InP}}/a_{\mathrm{Subst}}^{\mathrm{InAs}} = 0.9787 \pm 0.001$ (see also the Table 1). It was difficult to assess accurately $c_{\mathrm{NW}}^{\mathrm{InP}}$ due to the low experimental resolution used in CTR measurements and to the low signal, but for InAs, we measured $c_{\mathrm{NW}}^{\mathrm{InAs}} \approx a_{\mathrm{NW}}^{\mathrm{InAs}}/\sqrt{2}$. Note that no clear signals due to the NW superlattice periodicity have been measured in these experiments. It may be due to several reasons, the effects of which are probably combined: strain relaxation distribution along the NWs, disorientations, section variations induced by the catalyst particle's diameter distribution and growth fluctuations (the

Table 1. Calculated Averaged In-Plane Deformation $\langle \epsilon_{yy} \rangle$ for Nanowire Superlattices with Radius $R = 22$ nm Consisting of 20 nm InAs/7 or 10 nm InP Layers[a]

		20 nm InAs/ 7 nm InP NW	20 nm InAs/ 10 nm InP NW
$\langle \epsilon_{yy} \rangle$ (%)	InAs (-0.64 ± 0.1):	-0.46	-0.61
	InP (-2.13 ± 0.1):	-1.82	-2.15
σ_{yy} (%)	InAs:	0.37	0.42
	InP:	0.50	0.43

[a] The atomic positions are relaxed with the valence force field described in the text. The deformations are calculated with respect to the cubic InAs reference and the experimental values are parenthesized. The standard deviations (σ_{yy}) of these deformations show the intrinsic broadening of this longitudinal nanowire structure.

longitudinal growth rate, and therefore the insertion thickness, varies with the NW diameter), or to a height (i.e., phase) shift coming from a nucleation delay before the beginning of the growth of individual NW.

The diffraction peak broadening may have several origins: (i) the NW size along the momentum transfer, (ii) the NW mosaicity corresponding to the in-plane (twist) and out-of-plane (tilt) rotations of the individual NWs, (iii) a nonuniform strain field with a local lattice parameter variation, including heterostructure strain relaxation and bending of the growth axis. (ii) and (iii) depend on the modulus of the momentum transfer, whereas (i) does not.

In-plane mosaicity is measured from transverse scans along (h00) reflections (rocking scan of the sample along its surface normal). It gives a full width at half-maximum (fwhm of a Gaussian function) of the TW peaks lower than 0.02°, whereas the NW peaks have an in-plane mosaicity of about 0.5 ± 0.1°. The fwhm of in-plane radial scans along [h00] (for example, for the relaxed InAs peak of Figure 4a) is 0.143 ± 0.006 nm^{-1}, which can be attributed to a NW cross-section diameter between hexagonal facets of about 44 ± 2 nm. This value, consistent with Figure 1, will be confirmed by SAXS measurements below.

The experimental results can be compared to atomistic simulations. We consider hexagonal [0001]-oriented InAs/InP nanowires superlattices with the wurtzite structure. The edge length (and radius) of the regular hexagon ($\{10\bar{1}0\}$ facets in hexagonal notation) is $R = 22$ nm, and the period of the superlattice is $l \approx 30$ nm. The thickness of the InAs layer is 20 nm, while the thickness of the InP layer is varied from 7 to 10 nm. The relaxed atomic positions are computed using Keating's valence force field (VFF model).[10] In this model, the elastic energy depends on the nearest-neighbor bond lengths and bond angles through bond stretching and bond bending constants. These parameters are fitted to the bulk modulus and Poisson ratio ν_{111} of the zinc-blende materials,[11−12] assuming that the elastic constants of the wurtzite phases fulfill Martin's relations.[13] The elastic energy is then minimized with respect to the atomic positions and period of the superlattice using a conjugate gradients algorithm, and the strain tensor is computed from the atomic positions in the $x = [2\bar{1}\bar{1}0]$, $y = [01\bar{1}0]$, and $z = [0001]$ axis set. Within this axis set, the k scans of GIXRD correspond to the y direction perpendicular to the hexagonal facets.

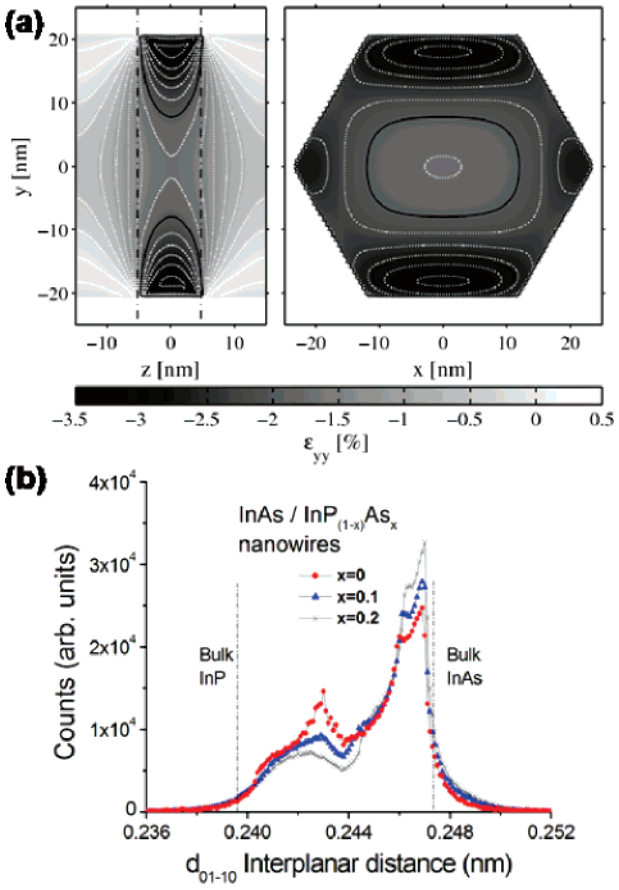

Figure 5. (a) In-plane deformations ϵ_{yy} (with reference to bulk InAs) for a 20 nm InAs/10 nm InP nanowires superlattice (cross sections at $x = 0$ and $z = 0$, respectively). The atomic positions are relaxed with the valence force field model described in the text. The black line is $\epsilon_{yy} = -2\%$, the difference between white dotted lines being $\Delta\epsilon_{yy} = 0.25\%$. (b) Histogram of the distances between $(01\bar{1}0)$ planes (perpendicular to the y direction; i.e., parallel to the hexagonal facets) for a 20 nm InAs/10 nm $InAs_xP_{1-x}$ nanowires superlattices with $x = 0$, 0.1, 0.2.

The in-plane deformation ϵ_{yy}, computed with reference to bulk InAs,[15] is shown in Figure 5a for the 20 nm InAs/10 nm InP structure. The InP layer, whose elastic constants are close to InAs, is heavily compressed by the latter. The surface of the nanowires can, however, bulge to relieve part of the stresses, which leads to a very inhomogeneous strain distribution (see for example refs 12 and 14 for a discussion of the electronic and optical properties of InAs/GaAs nanowire superlattices). The average in-plane deformations in InAs and InP are reported in Table 1 for two InP thicknesses (7 and 10 nm). The standard deviations of these values are very large even for ideal objects, indicating that the strain inhomogeneity is an intrinsic source of the peak broadening observed in GIXRD. These distributions must be taken into account to optimize band gap strain engineering in complex heterostructures. The strains are, moreover, very close to those computed in similar zinc-blende nanowire superlattices.

The calculated average in-plane deformations in InAs and InP (inside the 20 nm InAs/10 nm InP NW superlattice) are in very good agreement with the experimental values parenthesized in Table 1. The impact of various structural

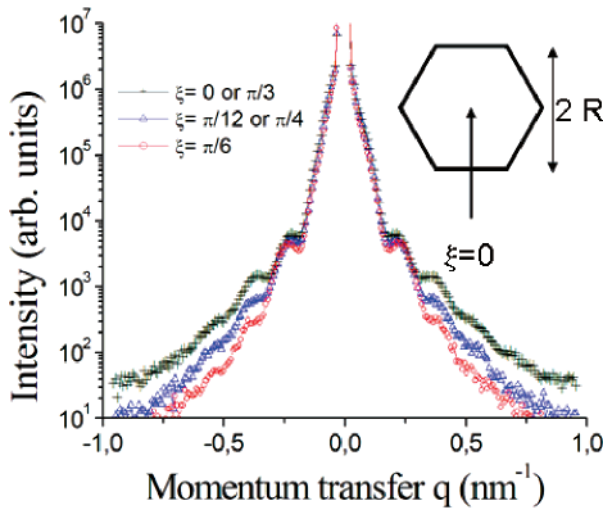

Figure 6. Small-angle X-ray scattering measurements for several azimuth ξ (see inset for definition) as the function of the momentum transfer $q = 4\pi \sin(\theta)/\lambda$ (θ is half of the scattered angle, λ is the wavelength). Grazing and emergence angles are very low (a few hundredths of a degree). Only three measurements (i.e., azimuths) are drawn, representative of the $\pi/6$ symmetry of the scattered intensity.

parameters (thickness of the InP layer, presence of an InAs shell, interdiffusion) has been investigated. The deformations in thinner (7 nm) InP layers are actually too small. The calculated deformations in core/shell 20 nm InAs/10 nm InP NW superlatices remain quite close: for a 1 nm thick InAs shell around a core with radius $R = 21$ nm, we get $\langle\epsilon_{yy}\rangle_{InAs} = -0.60\%$ and $\langle\epsilon_{yy}\rangle_{InP} = -2.04\%$, while for a 2 nm thick shell around a core with radius $R = 20$ nm, we get $\langle\epsilon_{yy}\rangle_{InAs} = -0.57\%$ and $\langle\epsilon_{yy}\rangle_{InP} = -1.94\%$. The interdiffusion is very limited for the low-temperature growth used in this study (390 °C): TEM energy dispersive spectrometry experiments estimate that the P atom concentration in InAs is lower than 2% (i.e., the noise level). For higher growth temperature, the influence of the substitution of P atoms by As in the InP layer (i.e., the insertion material) can be assessed by the distance between the $(01\bar{1}0)$ planes parallel to the nanowires edge (i.e., perpendicular to the k direction). Figure 5b gives the histogram of this distribution for 20 nm InAs/10 nm $InAs_xP_{1-x}$ superlattices with $x = 0$, 0.1, 0.2. It shows that a small substitution of P atoms largely shifts and broadens the initially "peaked" InP contribution, which can also contribute to an increase of the width of the in-plane diffraction peaks. Experimentally, the separation of interdiffusion and elastic relaxation contributions should be obtained by X-ray anomalous measurements around the As k absorption edge (11.868 keV).

After having analyzed the in-plane deformation with X-ray diffraction, we can also access to the average NW shape and size of this assembly by using small-angle X-ray scattering (SAXS)[15] at very grazing incidence and emergence ($\alpha = \beta \approx 0.1°$). Figure 6 shows selected intensity measurements $I(q)$ as a function of the in-plane scattering vector q for several sample orientations (azimuth) around the surface normal. Contrary to what is measured for cylindrical cross sections, we observe the dependence on the azimuth ξ of the

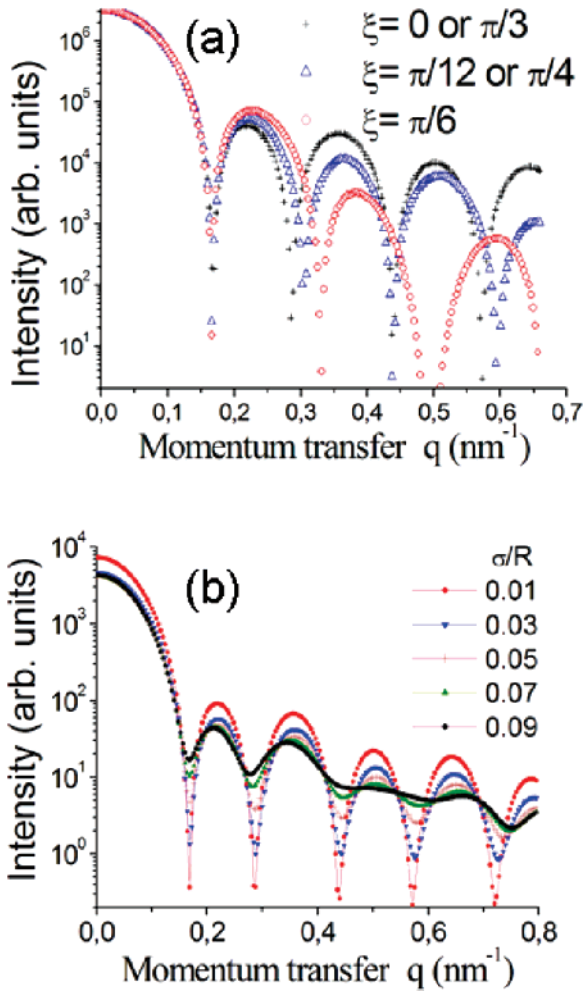

Figure 7. (a) DWBA calculation[10] of the in-plane intensity scattered by uncorrelated regular hexagonal NW of radius $R = 22$ nm at grazing incidence and emergence angles ($\alpha = \beta = 0.1°$). No size distribution is included in these calculations, and the azimuth ξ is defined by the inset of Figure 6. (b) Small-angle intensity calculated at $\xi = 0$ for a Gaussian distribution of the radius R of hexagonal NW. σ is the standard deviation of the R distribution ($\exp[-(x - x_0)^2/(2\sigma^2)]/[(2\pi)^{1/2}\sigma]$), and σ/R indicates the broadening.

oscillation fringes due to the NW size in a direction perpendicular to the beam both in position and intensity. The origin $\xi = 0$ is defined by a direction perpendicular to the NW facets (k direction in the diffraction experiments), as shown in the inset of Figure 6. The systematic measurement of $I(q)$ as a function of ξ (over $\pi/2$, every $\pi/36$) has shown a $\pi/6$ symmetry. The main features of the azimuth−angle dependence consist of the damping and the shift of the second-order fringe from $\xi = 0$ to $\pi/6$ and of the disappearance of the third oscillation at $\xi = \pi/6$. The center part of the experimental curve comes from the surface and overgrowth scattering. Note that in this sample, the NW density is very low (only about 2.5 NWs/μm^2 from Figure 1) so that synchrotron radiation is necessary. For higher densities, this method should be applied with a laboratory setup. Because no interparticle−position interactions have to be considered (see Figure 1c where the distribution of distances between nearest-neighbors NWs is very broad), the X-ray pattern can be analyzed as a convolution of the NW form factor by the

size distribution function. This form factor, derived in the simplest approximation from the Fourier transform of the NW shape,[15−17] can be calculated with the DWBA for a regular hexagon of height H and facet width R. As seen in Figure 7a, all the main features of the experimental measurements can be simulated by a monodisperse size distribution with $R = 22$ nm. The sharp interferences fringes appearing at roughly $q_{||} \sim 2\pi/R$ are associated to the zero of the sine cardinal or Bessel function for simple shapes like parallelepiped or cylinder. As observed in electron microscopy, the growth distribution involves both size and shape variations of the hexagonal cross sections with eventually a variation along the wire length. In a first approximation, only the R variation will be considered, giving a fringe smoothening with the increase of the width of the size distribution. This distribution can be modeled by a Gaussian function (fwhm σ) in the DBDA calculations. The calculated intensity for $\xi = 0$ is drawn in Figure 7b as a function of σ/R. Because the experimental measurements still show the third oscillation fringe, the maximum of the size distribution can be roughly estimated to be lower than $\sigma/R < 8\%$. This variation is mainly imposed by the aerosol particle size distribution and by fluctuations of the catalyst-assisted growth. More accurate measurements with 2D detectors in the grazing incidence SAXS geometry are presently under way to decrease the error bars and to study facets distribution.

In summary, this letter demonstrates the interest of X-ray grazing incidence techniques to get quantitative structural information on epitaxial NWs assemblies. The change of grazing incidence angle in surface diffraction experiments allows separating the different contributions of the signal, i.e., the nanowires from parasitic substrate overgrowths. More generally, these methods could be advantageous when studying samples grown by molecular beam epitaxy, which is a less selective growth method, leading to a larger overgrowth at the nanowires base. The crystalline phases (cubic or hexagonal) as well as growth defects (stacking faults) are determined from the direct analysis of crystal truncation rods. In the present study, the InAs/InP heterostructure was entirely hexagonal with equivalent variants, and a second twinned phase is present only as a substrate overgrowth. The same method could also be applied to inhomogeneous NW (for example GaAs) having a mixture of hexagonal and cubic phases. The in-plane epitaxial disorientations of the NW are small (fwhm $\approx 0.5°$), indicating a very good control of the initial growth stage consistent with classical mosaicity observed in metal (aerosol)/semiconductor substrate epitaxy. The strain distribution resulting from the relaxation in the NW geometry, measured from the position and broadening of the diffraction peaks, is in agreement with atomistic calculations of ideal structures. Complementary experiments using small-angle scattering have shown the possibility to check the size and shape of the objects. This method seems to be very promising in homogeneous assemblies to estimate such geometrical fluctuations, in particular with colloid-assisted growth, where synchrotron experiments are not necessary for dense assemblies. Last, grazing incidence X-ray techniques can be developed to study and to optimize the NW growth mechanisms or the technological processes. They will be helpful to integrate well-controlled NW building blocks into functional assemblies, and ultimately into systems.

Acknowledgment. This work has been performed under the EU program NODE 015783. We thank the French CRG-IF and ID01 ESRF beamlines for their technical help.

References

(1) Bell, D. C.; Wu, Y.; Barrelet, C. J.; Gradečak, S.; Xiang, J.; Timko, B. P.; Lieber, C. M. *Microsc. Res. Techn.* **2004**, *64*, 373.
(2) Johansson, J.; Karlsson, L. S.; Swensson, C. P. T.; Mårtensson, T.; Wacaser, B. A.; Deppert, K.; Samuelson, L.; Seifert, W. *Nat. Mater.* **2006**, *5*, 574.
(3) Bakkers, E. P. A. M.; Van Dam, J. A.; De Franceschi, S.; Kouwenhoven, L. P.; Kaiser, M.; Verheijen, M.; Wondergem, H.; Van Der Sluis, P. *Nat. Mater.* **2004**, *3*, 769.
(4) Svensson, C. P. T.; Seifert, W.; Larsson, M. W.; Wallenberg, L. R.; Stangl, J.; Bauer G.; Samuelson, L. *Nanotechnology* **2005**, *16*, 936.
(5) Kawamura, T.; Bhunia, S.; Watanabe, Y.; Fujikawa, S.; Matsui, J.; Kagoshima, Y.; Tsusaka, Y. *J. Appl. Phys.* **2005**, *97*, 084318.
(6) Mandl, B.; Stangl, J.; Märtensson, T.; Mikkelsen, A.; Eriksson, J.; Karlsson, L. S.; Bauer, G.; Samuelson L.; Seifert, W. *Nano Lett.* **2006**, *6*, 1817.
(7) Metzger, T. H.; Schülli, T. U.; Schmidbauer, M. *C. R. Phys.* **2005**, *6*, 47.
(8) Larsson, M. W.; Wagner, J. B.; Wallin, M.; Håkansson; Fröberg, L. E.; Samuelson, L.; Wallenberg, L. Reine *Nanotechnology* **2007**, *18*, 015504.
(9) Rauscher, M.; Panagio, R.; Metzger, H.; Kovats, Z.; Domke, J.; Peisl, J.; Pfannes, H. D.; Schulze, J.; Eisele, I. *J. Appl. Phys.* **1999**, *86*, 6763.
(10) Keating, P.-N. *Phys. Rev.* **1966**, *145*, 637.
(11) Niquet, Y.-M. *Phys. Rev. B* **2006**, *74*, 155304.
(12) *Physics of Group IV Elements and III-V Compounds*, Madelung, O., Schulz, M., Weiss, H., Eds.; Landolt-Börnstein, New Series, Group III, Vol. 17, Part A; Springer-Verlag: New York, 1982.
(13) Martin, R. M. *Phys. Rev. B* **1972**, *6*, 4546.
(14) Niquet, Y.-M. *Nano Lett.* **2007**, *7*, 1105.
(15) Lazzari, R. *J. Appl. Crystallogr.* **2002**, *35*, 406.
(16) Vargas, R.; Louër, D.; Langford, J. I. *J. Appl. Crystallogr.* **1983**, *16*, 512.
(17) Boulle, A.; Conchon, F.; Guinebretière, R. *Acta Crystallogr., Sect. A: Found. Crystallogr.* **2006**, *A62*, 11.

NL070888Q